Solar Physics
DOI: 10.1007/•••••-•••-•••-••••-•

A Note on Computation of Relative Magnetic Helicity Flux Across the Photosphere

Yang Liu[1] · **P.W. Schuck**[2]

Abstract

A number of investigations of the rate of relative magnetic-helicity transport across the photosphere $[\, \mathrm{d}H/\mathrm{d}t|_S \,]$ have reported differences in the estimates computed from two different formulations of the relative-helicity flux density proxy $[\, G_A \,]$ and $[\, G_\theta \,]$. There have been suggestions that $[\, G_\theta \,]$ is a more robust helicity-flux density proxy and that the differences in the estimates of $[\, \mathrm{d}H/\mathrm{d}t|_S \,]$ are caused by biases in $[\, G_A \,]$, noise, and/or the boundary conditions. In this note, we prove that the differences are caused by the inconsistent choice of boundary conditions in the explicit or implicit Green's function $[\, \mathcal{G}(\mathbf{x}, \mathbf{x}') \,]$ used for computing $[\, G_A \,]$ and $[\, G_\theta \,]$ when comparing the helicity flux estimates based on $[\, G_A \,]$ and $[\, G_\theta \,]$. When the boundary conditions in $[\, \mathcal{G} \,]$ are chosen consistetently, the two helicity-flux density proxies, $[\, G_A \,]$ and $[\, G_\theta \,]$, produce essentially identical results for the rate of helicity transport across the photosphere. They also yield essentially identical results for the rate of helicity transport of the shearing and advection terms separately. Using MHD simulation, HMI observational data, and Monte Carlo simulations of noise we show that this result is robust. Neither the shape of the active region, nor the shape of the boundary, nor data noise causes any difference in the rate of helicity transport computed via $[\, G_A \,]$ and $[\, G_\theta \,]$.

Keywords: Solar magnetic field; Magnetic helicity; Helicity flux density

1. Introduction

Magnetic helicity in a solar active region is an useful parameter to describe complexity of this active region. Quantifying the magnetic-helicity flux across the photosphere is one way to measure the helicity that is accumulated in the corona. The relative magnetic helicity (for simplicity, hereafter we use magnetic

[1] W. W. Hansen Experimental Physics Laboratory, Stanford University, Stanford, CA 94305-4085, USA email: yliu@sun.stanford.edu,
[2] Space Weather Laboratory, NASA Goddard Space Flight Center, Greenbelt, MD 20771, USA email: peter.schuck@nasa.gov,

helicity to refer to relative magnetic helicity) flux across a surface S can be computed with the following equation (Berger, 1984),

$$\left.\frac{\mathsf{d}H}{\mathsf{d}t}\right|_S = 2\int_S \mathsf{d}S\left[\left(\mathbf{A}_p\cdot\mathbf{B}_t\right)v_n - \left(\mathbf{A}_p\cdot\mathbf{v}_t\right)B_n\right], \tag{1}$$

where $\mathbf{B}_t$ and B_n denote the tangential and normal magnetic fields, and $\mathbf{v}_t$ and v_n are the tangential and normal velocities, respectively. The first term represents the helicity flux across the surface S due to advection of twisted magnetic-flux tubes (emergence-term hereafter), and the second term due to the photospheric shear motion that shears and braids the field lines (shear-term hereafter) (Berger, 1984; Kusano *et al.*, 2002; Nindos *et al.*, 2003; Pevtsov *et al.*, 2003; Pariat *et al.*, 2005; Démoulin, 2007). The vector potential $[\ \mathbf{A}_p\ ]$ of the potential field having the same normal magnetic field is uniquely determined by the observed photospheric normal magnetic field and Coulomb gauge by (Berger and Ruzmaikin, 2000),

$$\nabla\times\mathbf{A}_p\cdot\widehat{\mathbf{n}} = B_n, \nabla\cdot\mathbf{A}_p = 0, \mathbf{A}_p\cdot\widehat{\mathbf{n}} = 0. \tag{2}$$

Consequently, the vector potential admits the Helmholtz decomposition

$$\mathbf{A}_p = -\nabla\times\left(\widehat{\mathbf{n}}\,\psi\right) \tag{3}$$

and $\widehat{\mathbf{n}}\cdot\nabla\times\mathbf{A}_p$ leads to the Poisson equation

$$\nabla_t^2\psi = B_n, \tag{4}$$

which has the general solution

$$\psi\left(\mathbf{x}\right) = \int_{S'}\mathsf{d}S'\,B_n\left(\mathbf{x}'\right)\,\mathcal{G}\left(\mathbf{x},\mathbf{x}'\right), \tag{5}$$

where

$$\nabla_t^2\mathcal{G}\left(\mathbf{x},\mathbf{x}'\right) = \delta\left(\mathbf{x}-\mathbf{x}'\right), \tag{6}$$

leading to an equation for the vector potential of the form

$$\mathbf{A}_p\left(\mathbf{x}\right) = \widehat{\mathbf{n}}\times\int_{S'}\mathsf{d}S'\,B_n\left(\mathbf{x}'\right)\,\nabla_t\mathcal{G}\left(\mathbf{x},\mathbf{x}'\right). \tag{7}$$

Equations (2 – 7) hold for spherical (Bogomolov, 1979; Kimura and Okamoto, 1987), planar (Berger and Ruzmaikin, 2000; Chae, 2001), and other geometries. However, Equations (4-7) are only part of the story. The problem is not completely specified until the geometry and the boundary conditions on the Green's function $\mathcal{G}\left(\mathbf{x},\mathbf{x}'\right)$ have been specified. Consistent boundary conditions are critical when comparing the helicity fluxes computed for different helicity-flux densities.

By introducing the flux transport velocity $[\ \mathbf{u}\ ]$, defined as,

$$\mathbf{u} = \mathbf{v}_t - \frac{v_n}{B_n}\mathbf{B}_t, \tag{8}$$

Equation (1) is simplified to be (Démoulin and Berger, 2003)

$$\left.\frac{\mathsf{d}H_A}{\mathsf{d}t}\right|_S = -2\int_S \mathsf{d}S\,(\mathbf{u}\cdot\mathbf{A}_p)\,B_n. \tag{9}$$

The corresponding proxy of helicity flux density across the surface S is then

$$G_A(\mathbf{x}) = -2\,(\mathbf{u}\cdot\mathbf{A}_p)\;B_n. \tag{10}$$

Pariat *et al.* (2005) suggested an alternative method for computing the helicity flux in a planar geometry

$$\left.\frac{\mathsf{d}H_\theta}{\mathsf{d}t}\right|_S = -\widehat{\mathbf{n}}\cdot\frac{1}{2\,\pi}\int_S \mathsf{d}S\int_{S'}\mathsf{d}S'\left\{\frac{\mathbf{x}-\mathbf{x}'}{|\mathbf{x}-\mathbf{x}'|^2}\times[\mathbf{u}(\mathbf{x})-\mathbf{u}(\mathbf{x}')]\right\}B_n(\mathbf{x})\;B_n(\mathbf{x}'), \tag{11}$$

where $\mathbf{x}$ and $\mathbf{x}'$ represent two photospheric positions, and $\widehat{\mathbf{n}}$ is the surface normal pointing into the corona. This way, the helicity flux density (proxy) across the surface S can be expressed as,

$$G_\theta(\mathbf{x}) = -\widehat{\mathbf{n}}\cdot\frac{B_n(\mathbf{x})}{2\,\pi}\int_{S'}\mathsf{d}S'\left\{\frac{\mathbf{x}-\mathbf{x}'}{|\mathbf{x}-\mathbf{x}'|^2}\times[\mathbf{u}(\mathbf{x})-\mathbf{u}(\mathbf{x}')]\right\}B_n(\mathbf{x}'). \tag{12}$$

In principle, surface integrals over G_A or G_θ are equivalent. And indeed, it is only these surface integrals which correspond to gauge invariant observables — the helicity flux density is not unique. Pariat *et al.* (2005) noted that neither G_A nor G_θ represent the true helicity flux density, but showed that G_A exhibits much stronger fake polarities using simple modeled fields and plasma flows. They suggested that the "fake polarities induced by G_A could represent significant, if not dominant, contributions to the observed positive and negative flux of magnetic helicity, maybe even masking the real helicity flux injection" (Pariat *et al.*, 2005)[1]. In a practical study of five active regions observed by *SOHO*/MDI (Scherrer *et al.*, 1995), Pariat *et al.* (2006) computed the G_A via padded the Fast Fourier Transform (FFT) by embedding the data in maps two – three times larger to minimize boundary effects while computing G_θ from equation (12). They found differences of up to 15 % for the helicity fluxes computed from G_A and G_θ. They attributed the differences to "the larger errors in $\mathrm{d}H_A/\mathrm{d}t$ measurement due to the intense fake signals that G_A produces." They also suggested that noise makes some contribution to the differences. Similarly, Jeong and Chae (2007) and Chae (2007) found differences between values of $\mathrm{d}H_A/\mathrm{d}t|_S$ calculated via FFT and $\mathrm{d}H_\theta/\mathrm{d}t|_S$ from equation (12) by a factor of 10 % – 30 %. They suggested that the effect of the spatially periodic boundary outside of the region used in FFT for calculating G_A causes this difference, and speculated that these results should be identical if the domain of the FFT were extended to infinity. Finally, Welsch *et al.* (2007) in their study of velocity estimation algorithms with MHD

[1]The average value of G_A could be about 70% higher than that of G_θ (Romano *et al.*, 2012).

data noted that $\mathrm{d}H_A/\mathrm{d}t|_S$ and $\mathrm{d}H_\theta/\mathrm{d}t|_S$ were equal when G_A was computed using the free-space Green's function for $\mathbf{A}_p$.

While researchers skilled in the art seemed to have reached the conclusion that quantitative differences between computed estimates of $\mathrm{d}H_A/\mathrm{d}t|_S$ and $\mathrm{d}H_\theta/\mathrm{d}t|_S$ are probably caused by boundary conditions, to our knowledge there has been no formal proof or demonstration that G_A and G_θ produce identical results. Nor does this conclusion appear to be common knowledge. Indeed, there are at least some researchers who are convinced that G_θ provides a superior estimate of the helicity flux.

In this note, we use theory, MHD simulation data, and observational data to explore the discrepancy between helicity flux estimates. Our analysis shows that boundary condition on the Green's function $\mathcal{G}$ used to compute the helicity flux density is the true cause of the differences. The fake polarities and data noise do not produce any significant differences for the helicity flux computed either from G_A or from G_θ. When the boundary conditions on $\mathcal{G}$ are chosen consistetently, the two helicity fluxes from G_A and G_θ produce essentially identical results for the rate of helicity transport across the photosphere.

The note is organized as follows. Section 2 recasts G_θ as a Green's function problem and equivalence between $\mathrm{d}H_A/\mathrm{d}t|_S$ and $\mathrm{d}H_\theta/\mathrm{d}t|_S$ is proven when the Green's function is chosen consistently. Using the Green's function formalism, a periodic form of G_θ based on a manifestly periodic Green's function is derived appropriate for use with the FFT. This permits both G_A and G_θ to be computed precisely using either free-space or periodic boundary conditions. Section 3 describes the data used and tests conducted. The data used are MHD simulation data and observational data taken by HMI (Scherrer *et al.*, 2012; Schou *et al.*, 2012) onboard *SDO* (Pesnell *et al.*, 2012). We compute both G_A and G_θ using both free-space and periodic boundary conditions. Tests are also done by changing the boundary shape and adding noise to the data in order to examine their effects on computing the helicity flux. The results are presented in Section 4, and summarized in Section 5.

2. Recasting G_θ as a Green's Function Problem

Equation (12) may be rewritten as

$$G_\theta\left(\mathbf{x}\right) = B_n\left(\mathbf{x}\right)\,\widehat{\mathbf{n}}\cdot\int_{S'}\mathrm{d}S'\,B_n\left(\mathbf{x}'\right)\,\left[\mathbf{u}\left(\mathbf{x}\right)-\mathbf{u}\left(\mathbf{x}'\right)\right]\times\nabla_t\frac{\ln\left|\mathbf{x}-\mathbf{x}'\right|}{2\,\pi}. \tag{13}$$

where the two-dimensional free-space Green's function may be identified as

$$\mathcal{G}_{\mathrm{FS}}\left(\mathbf{x},\mathbf{x}'\right) = \frac{\ln\left|\mathbf{x}-\mathbf{x}'\right|}{2\,\pi}. \tag{14}$$

This form of the Green's function in Eq. (13) results from a specific choice of geometry (planar) and a specific choice of free-space boundary conditions in Eq. (5), namely, $\mathcal{G}\left(\mathbf{x},\mathbf{x}'\right)\rightarrow 0$ as $\left|\mathbf{x}-\mathbf{x}'\right|\rightarrow\infty$. Thus, G_θ may be generalized as

$$G_\theta\left(\mathbf{x}\right) = B_n\left(\mathbf{x}\right)\,\widehat{\mathbf{n}}\cdot\int_{S'}\mathrm{d}S'\,B_n\left(\mathbf{x}'\right)\,\left[\mathbf{u}\left(\mathbf{x}\right)-\mathbf{u}\left(\mathbf{x}'\right)\right]\times\nabla_t\mathcal{G}\left(\mathbf{x},\mathbf{x}'\right), \tag{15}$$

or

$$G_\theta(\mathbf{x}) = \frac{G_A(\mathbf{x})}{2} - B_n(\mathbf{x})\,\widehat{\mathbf{n}} \cdot \int_{S'} \mathsf{d}S'\, B_n(\mathbf{x}')\,\mathbf{u}(\mathbf{x}') \times \nabla_t \mathcal{G}(\mathbf{x},\mathbf{x}')\,. \tag{16}$$

where $\mathcal{G}(\mathbf{x},\mathbf{x}')$ represents a spherical or planar Green's function with boundary conditions sufficient for Eq. (5) to be a unique solution of Eq. (4) on the field-of-view.

2.1. Proof that $\mathrm{d}H_A/\mathrm{d}t|_S$ and $\mathrm{d}H_\theta/\mathrm{d}t|_S$ are Equivalent

Adding and subtracting $G_A(\mathbf{x})/2$ we obtain a simple expression for $G_\theta(\mathbf{x})$

$$G_\theta(\mathbf{x}) = G_A(\mathbf{x}) + \Delta(\mathbf{x})\,, \tag{17}$$

where

$$\Delta(\mathbf{x}) = -B_n(\mathbf{x})\,\widehat{\mathbf{n}} \cdot \int_{S'} \mathsf{d}S'\, B_n(\mathbf{x}')\,\mathbf{u}(\mathbf{x}') \times \nabla_t \mathcal{G}(\mathbf{x},\mathbf{x}') - \frac{G_A(\mathbf{x})}{2}. \tag{18}$$

Re-expanding G_A we have

$$\begin{aligned}\Delta(\mathbf{x}) \;=\; & -B_n(\mathbf{x})\,\widehat{\mathbf{n}} \cdot \left[\int_{S'} \mathsf{d}S'\, B_n(\mathbf{x}')\,\mathbf{u}(\mathbf{x}') \times \nabla_t \mathcal{G}(\mathbf{x},\mathbf{x}') \right.\\ & \left. + \mathbf{u}(\mathbf{x}) \times \int_{S'} \mathsf{d}S'\, B_n(\mathbf{x}')\,\nabla_t \mathcal{G}(\mathbf{x},\mathbf{x}')\right], \end{aligned} \tag{19}$$

with

$$\Sigma \;\equiv\; \int_S \mathsf{d}S\,\Delta(\mathbf{x}) \tag{20}$$

$$\begin{aligned} =\; & -\int_S \mathsf{d}S\, B_n(\mathbf{x})\,\widehat{\mathbf{n}} \cdot \left[\int_{S'} \mathsf{d}S'\, B_n(\mathbf{x}')\,\mathbf{u}(\mathbf{x}') \times \nabla_t \mathcal{G}(\mathbf{x},\mathbf{x}') \right.\\ & \left. + \mathbf{u}(\mathbf{x}) \times \int_{S'} \mathsf{d}S'\, B_n(\mathbf{x}')\,\nabla_t \mathcal{G}(\mathbf{x},\mathbf{x}')\right]. \end{aligned} \tag{21}$$

But now the integration variables are simply dummy variables, the primed and unprimed variables may be exchanged in the second integrand leading to

$$\begin{aligned}\Sigma \;=\; & -\widehat{\mathbf{n}} \cdot \left[\int_S \mathsf{d}S \int_{S'} \mathsf{d}S'\, B_n(\mathbf{x})\, B_n(\mathbf{x}')\,\mathbf{u}(\mathbf{x}') \times \nabla_t \mathcal{G}(\mathbf{x},\mathbf{x}') \right.\\ & \left. + \int_S \mathsf{d}S \int_{S'} \mathsf{d}S'\, B_n(\mathbf{x})\, B_n(\mathbf{x}')\,\mathbf{u}(\mathbf{x}') \times \nabla_t \mathcal{G}(\mathbf{x}',\mathbf{x})\right]. \end{aligned} \tag{22}$$

Noting that $\nabla_t \mathcal{G}(\mathbf{x}',\mathbf{x}) = -\nabla_t \mathcal{G}(\mathbf{x},\mathbf{x}')$ we have

$$\Sigma \equiv 0. \tag{23}$$

Thus, as long as a *consistent* Green's function is used to define both G_A and G_θ

$$\left.\frac{\mathsf{d}H_A}{\mathsf{d}t}\right|_S \equiv \left.\frac{\mathsf{d}H_\theta}{\mathsf{d}t}\right|_S \tag{24}$$

and extending this result to the shear and advection terms individually is trivial. Pariat *et al.* (2005) used the free-space Green's function [$\mathcal{G}_{\rm FS}$] to calculate G_θ and $\mathrm{d}H_\theta/\mathrm{d}t|_S$ and an effectively, manifestly periodic Green's function

$$\mathcal{G}_{\rm Periodic}\left(\mathbf{x},\mathbf{x}'\right) = -\frac{1}{L_x}\frac{1}{L_y}\sum_{p,q=-\infty}^{\infty}\frac{\mathsf{e}^{i\,2\,\pi\,p\left(x-x'\right)/L_x}\,\mathsf{e}^{i\,2\,\pi\,q\left(y-y'\right)/L_y}}{\left[\left(\frac{2\,\pi\,p}{L_x}\right)^2+\left(\frac{2\,\pi\,q}{L_y}\right)^2\right]}, \tag{25}$$

to compute G_A and $\mathrm{d}H_A/\mathrm{d}t|_S$ via the FFT. Here L_x and L_y are the physical width and height of the planarized field of view. Since the Green's functions (14) and (25) correspond to different assumptions about the behavior of $\mathbf{A}_p$ outside the field of view, it is no surprise that this led to that different quantitative estimates for $\mathrm{d}H_\theta/\mathrm{d}t|_S$ and $\mathrm{d}H_A/\mathrm{d}t|_S$ as computed by Pariat *et al.* (2006), Jeong and Chae (2007), and Chae (2007). However, when $\mathrm{d}H_\theta/\mathrm{d}t|_S$ and $\mathrm{d}H_A/\mathrm{d}t|_S$ are computed consistently, they produce identical results to the round-off error (see Section 4).

2.2. Fast Computation of G_θ

The Green's function formulation of G_θ in Equation (16) suggests a quick and dirty method for computing G_θ precisely via FFT convolution.

$$G_\theta\left(\mathbf{x}\right) = \frac{G_A\left(\mathbf{x}\right)}{2} - B_n\left(\mathbf{x}\right)\,\widehat{\mathbf{n}}\cdot\int_{S'}\mathsf{d}S'\,\mathbf{F}\left(\mathbf{x}'\right)\times\nabla_t\mathcal{G}\left(\mathbf{x},\mathbf{x}'\right) \tag{26}$$

where

$$\mathbf{F}\left(\mathbf{x}\right) \equiv B_n\left(\mathbf{x}\right)\,\mathbf{u}\left(\mathbf{x}\right) = \mathbf{F}_{\rm shear}\left(\mathbf{x}\right) + \mathbf{F}_{\rm adv}\left(\mathbf{x}\right), \tag{27}$$

is the flux-transport vector comprised of the shearing and advection terms respectively

$$\mathbf{F}_{\rm shear}\left(\mathbf{x}\right) = B_n\left(\mathbf{x}\right)\,\mathbf{v}_{\perp t}\left(\mathbf{x}\right), \tag{28}$$

$$\mathbf{F}_{\rm adv}\left(\mathbf{x}\right) = -v_{\perp n}\left(\mathbf{x}\right)\,\mathbf{B}_t\left(\mathbf{x}\right), \tag{29}$$

where the "$\perp$" subscript indicates that the irrelevant field-aligned plasma flow has been removed. Writing the flux-transport vector as a manifestly periodic function

$$\mathbf{F}\left(\mathbf{x}'\right) = \sum_{p',q'=-\infty}^{\infty}\tilde{\mathbf{F}}_{p'q'}\,\mathsf{e}^{i\,2\,\pi\,p'\,x'/L_x}\,\mathsf{e}^{i\,2\,\pi\,q'\,y'/L_y}, \tag{30}$$

and using the periodic Green's function in Equation (25), G_θ becomes

$$G_\theta\left(\mathbf{x}\right) = \frac{G_A\left(\mathbf{x}\right)}{2} + B_n\left(\mathbf{x}\right)\frac{2\,\pi\,i}{L_x\,L_y}\sum_{p,q=-\infty}^{\infty}\frac{\mathsf{e}^{i\,2\,\pi\,p\,x/L_x}\,\mathsf{e}^{i\,2\,\pi\,q\,y/L_y}}{\left(\frac{2\,\pi\,p}{L_x}\right)^2+\left(\frac{2\,\pi\,q}{L_y}\right)^2} \times \sum_{p',q'=-\infty}^{\infty}\widehat{\mathbf{n}}\cdot\tilde{\mathbf{F}}_{p'q'}\times\left(\frac{p}{L_x},\frac{q}{L_y}\right)\int_{S'}\mathsf{d}S'\mathsf{e}^{i\,2\,\pi\left[\left(p'-p\right)x'/L_x+\left(q'-q\right)y'/L_y\right]}. \tag{31}$$

Performing the integration over S' we have the simple expression

$$G_\theta\left(\mathbf{x}\right) = \frac{G_A\left(\mathbf{x}\right)}{2} + B_n\left(\mathbf{x}\right)\sum_{p,q=-\infty}^{\infty}\mathsf{e}^{i\,2\,\pi\left(\frac{p\,x}{L_x}+\frac{q\,y}{L_y}\right)}\left\{\frac{i\,\widehat{\mathbf{n}}\cdot\left[\tilde{\mathbf{F}}_{pq}\times\left(\frac{2\,\pi\,p}{L_x},\frac{2\,\pi\,q}{L_y}\right)\right]}{\left(\frac{2\,\pi\,p}{L_x}\right)^2+\left(\frac{2\,\pi\,q}{L_y}\right)^2}\right\}, \tag{32}$$

where the summation represents the inverse Fourier transform of the term in curly braces. Equation (32) is the precise periodic analog of Equation (12). This manifestly periodic version of G_θ is distinguished from previous work that forced periodic boundary conditions on the free-space Green's function by zero-padding data (Chae, 2007).

3. Data and Test

Simulation data from Welsch *et al.* (2007) and vector magnetic-field observations from HMI are used to test these conclusions. The MHD data used are described in detail by Welsch *et al.* (2007) and Abbett *et al.* (2000, 2004). These data are in Cartesian coordinates and for this test, the simulation vector magnetic field and velocity were used to compute the helicity density. Figure 1 shows the vector magnetic field from the MHD simulation. Information on HMI vector magnetic-field data can be found in Hoeksema *et al.* (2012), Sun *et al.* (2012), and Liu and Schuck (2012). For the HMI data, the vector velocity field is derived by applying the Differential Affine Velocity Estimator for Vector Magnetograms (DAVE4VM: Schuck, 2008) to the HMI time-series vector magnetic-field data. The window size is 19 pixels. The cadence of the HMI data used is 720 seconds. The active region chosen is AR 11072 at 12:00 UT 22 May 2010 when it was at S16W00 (see Liu and Schuck, 2012, for more details for this active region). The vector magnetic-field data were projected onto the heliographic coordinates using the Lambert (cylindrical equal area) projection method and is shown in Figure 2. The vector velocity in both cases has been further corrected by removing the irrelevant field-aligned plasma flow. This results in the velocities perpendicular to the field line, $\mathbf{v}_{\perp t}$ and $v_{\perp n}$, as described in Equations (28)-(29).

Both helicity flux density proxies G_A and G_θ are calculated using the MHD and HMI data. The proxies are then used to compute the total helicity flux, the shear-term and the emergence-term helicity fluxes. The shear-term and emergence-term helicity fluxes are related with $\mathbf{v}_{\perp t}$ and $v_{\perp n}$, respectively. We then examine any differences in the helicity fluxes via these two density proxies.

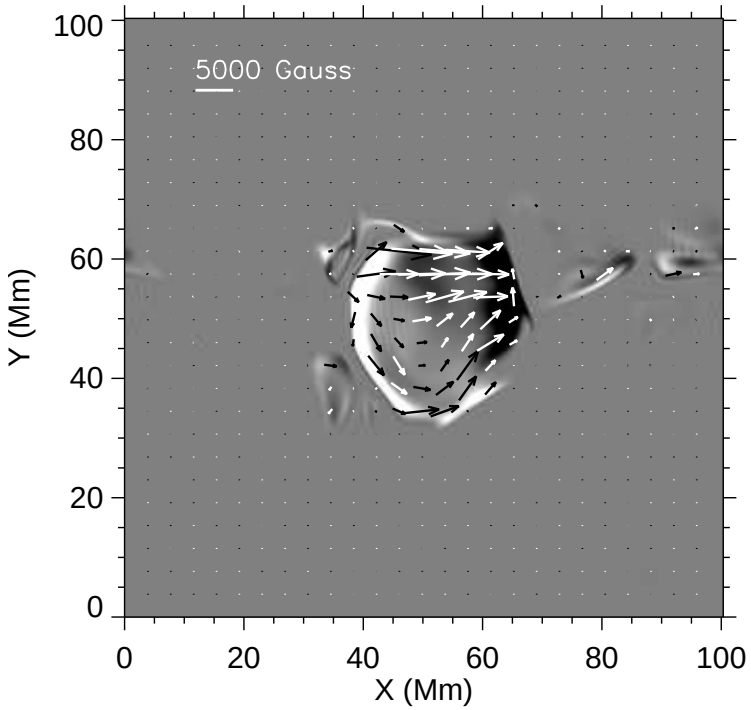

Figure 1. Vector magnetic field of the MHD data. The image is normal field with positive field in white and negative in black. It is scaled to ±1500.0 Gauss. The arrows represent tangential field. Black (white) arrows indicate that the normal fields at those pixels are positive (negative).

We choose two different boundary conditions on the Green's function to compute G_A and G_θ: the periodic Green's function $\mathcal{G}_{\rm Periodic}$ ($G_{\rm A-FFT}$ and $G_{\theta-FFT}$ hereafter) and the free-space Green's function $\mathcal{G}_{\rm FS}$ ($G_{\rm A-FS}$ and $G_{\theta-\rm FS}$ hereafter).

4. Results

Helicity flux density from the MHD data is presented in Figure 3. From top to bottom are $G_{\rm A-FFT}$, $G_{\rm A-FS}$, $G_{\theta-\rm FFT}$, and $G_{\theta-\rm FS}$, and from left to right are the total helicity flux density, helicity flux density from shear-term, and helicity flux density from emergence-term, respectively. Indeed, as Pariat *et al.* (2005) pointed out, both $G_{\rm A-FFT}$ and $G_{\rm A-FS}$ do contain intense fake signals, while they are greatly minimized in the $G_{\theta-\rm FFT}$ and $G_{\theta-\rm FS}$ maps. However, when integrated over the whole region to derive the helicity fluxes, $G_{\rm A-FFT}$ and $G_{\theta-\rm FFT}$ yield identical values for all three measures: total, shear-term, and emergence-term helicity fluxes (see Table 1). So do $G_{\rm A-FS}$ and $G_{\theta-\rm FS}$. The difference between the fluxes from $\mathcal{G}_{\rm Periodic}$ and $\mathcal{G}_{\rm FS}$ is about 9 %. This indicates that it is the boundary conditions on the Green's function chosen for computing the density proxies that caused that 10 – 30 % helicity flux differences in Pariat *et al.* (2006), Jeong and Chae (2007), and Chae (2007) – the total helicity fluxes compared in their papers were computed from $G_{\rm A-FFT}$ and $G_{\theta-\rm FS}$.

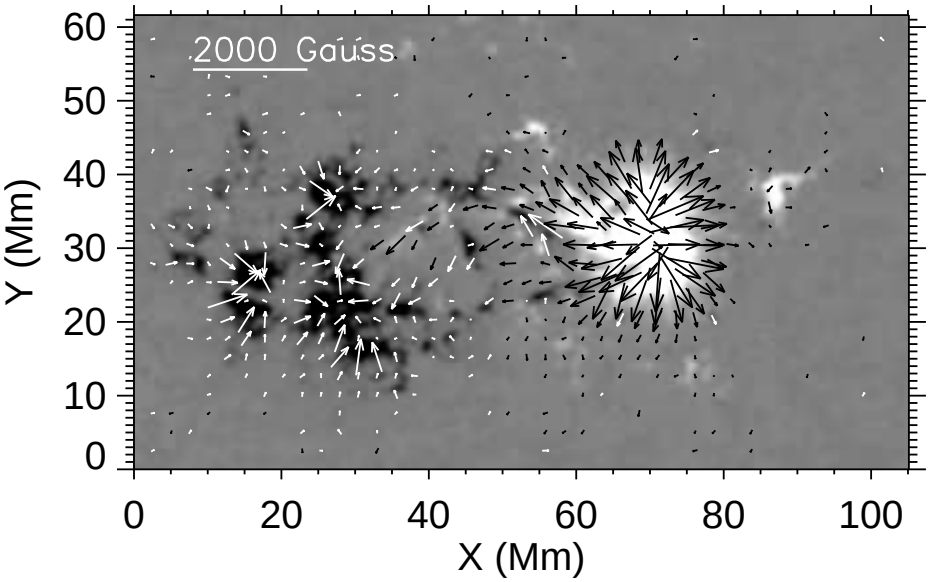

Figure 2. Vector magnetic field in active region AR 11072 at 12:00 UT on 22 May 2010. The image is normal field with positive field in white and negative in black. It is scaled to ±800.0 Mx cm^{-2}. The arrows represent tangential field. Black (white) arrows indicate that the normal fields at those pixels are positive (negative). The arrows at the pixels where the normal fields are less than 20.0 Mx cm^{-2} are not plotted.

Testing of data noise was also done with this set of data by conducting a Monte-Carlo simulation. In this test, we randomly added noise on each component of vector magnetic field and velocity field. The noises have a Gaussian distribution with a σ of 300 Gauss for magnetic field and 100 m s^{-1} for velocity field, respectively. The test shows that the helicity fluxes from both G_A and G_θ agree to machine precision as long as the boundary conditions on the Green's function are chosen consistently.

Testing of HMI data is shown in Figure 4. Again, both $G_{\mathrm{A-FFT}}$ and $G_{\mathrm{A-FS}}$ contain intense fake signals, especially in the leading sunspot. However, the helicity fluxes computed from $G_{\mathrm{A-FFT}}$ and $G_{\theta-\mathrm{FFT}}$ agree, and those from $G_{\mathrm{A-FS}}$ and $G_{\theta-\mathrm{FS}}$ agree; but the helicity fluxes from $\mathcal{G}_{\mathrm{Periodic}}$ and $\mathcal{G}_{\mathrm{FS}}$ differ by a factor of about 10 %.

Testing of irregular boundary shapes was conducted with this HMI data by setting vector magnetic and velocity fields to be zero in several ring-shape bands, as illustrated in the normal field map in Figure 5. All three measures of helicity fluxes, total, shear-term, and emergence-term fluxes from G_A and G_θ are identical when the boundary conditions are chosen consistently. This indicates that boundary shape does not cause any difference in computing helicity flux via these two methods.

Zero-padding data prior to applying the FFTs can approximate the computation of free-space quantities in the context of periodic boundaries (Pariat *et al.*, 2005; Chae, 2007). We embedded the original **B** and **V** data from the MHD simulation (the size is L_x (width) by L_y (height) of the planarized field of

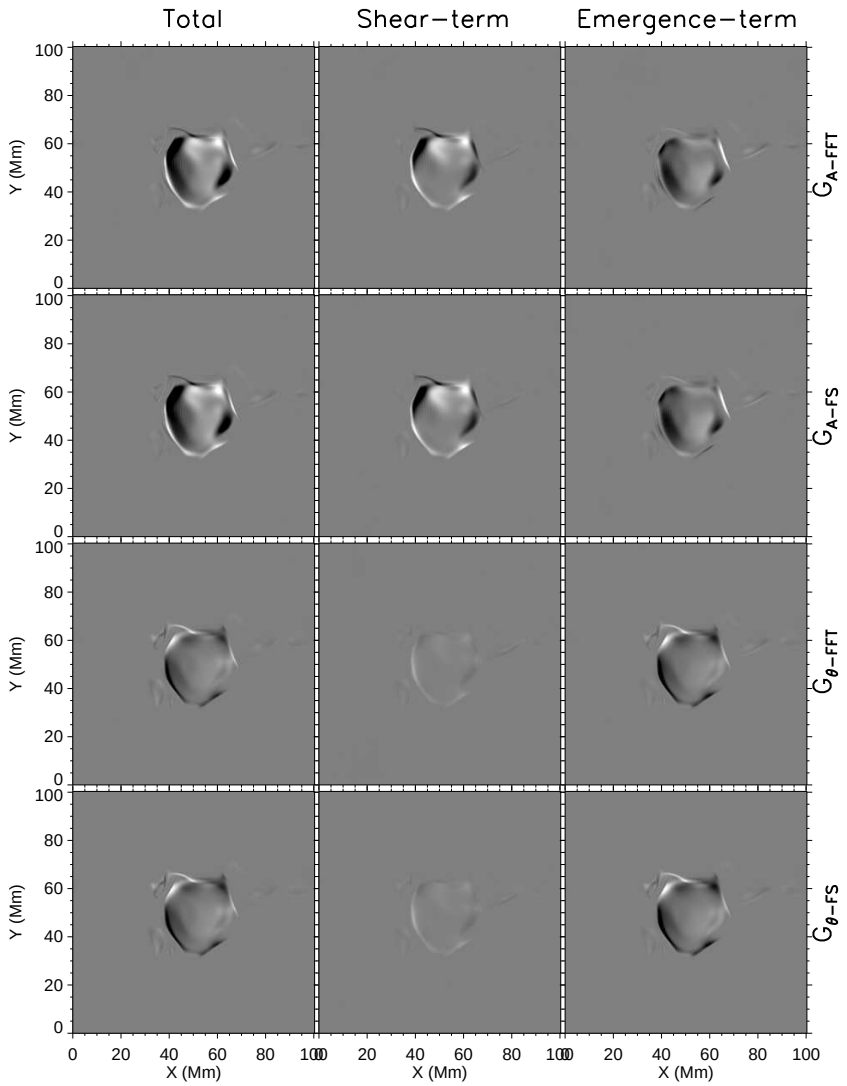

Figure 3. Helicity flux density for the MHD data. From top to bottom are $G_{\mathrm{A-FFT}}$, $G_{\mathrm{A-FS}}$, $G_{\theta-\mathrm{FFT}}$, and $G_{\theta-\mathrm{FS}}$. From left to right are total-helicity flux density, helicity flux density from shear-term, and helicity flux density from emergence-term, respectively. They are all scaled to $\pm 4.0\times10^{19}$ Mx^2 cm^{-2} s^{-1}.

view) in a new array with a size of $N \times L_x$ (width) by $N \times L_y$ (height), where $N = 1, 2, 3, ..., 12$. The elements outside of the embedded array are set to be zero for both $\mathbf{B}$ and $\mathbf{V}$. An approximation to the free-space vector potential $\mathbf{A}_p$ is computed from this augmented array via FFT and equations (3) and (4). Plotted in Figure 6 is helicity flux estimated from the helicity density $G^{\mathrm{FFT}}_{\mathrm{A-FS}}$ computed from this approximate free-space vector potential as a function of N (the solid line with asterisks). As a reference, we also plot with dashed line the helicity flux from $G_{\mathrm{A-FS}}$ computed directly from Equation (9) with free-space Green's

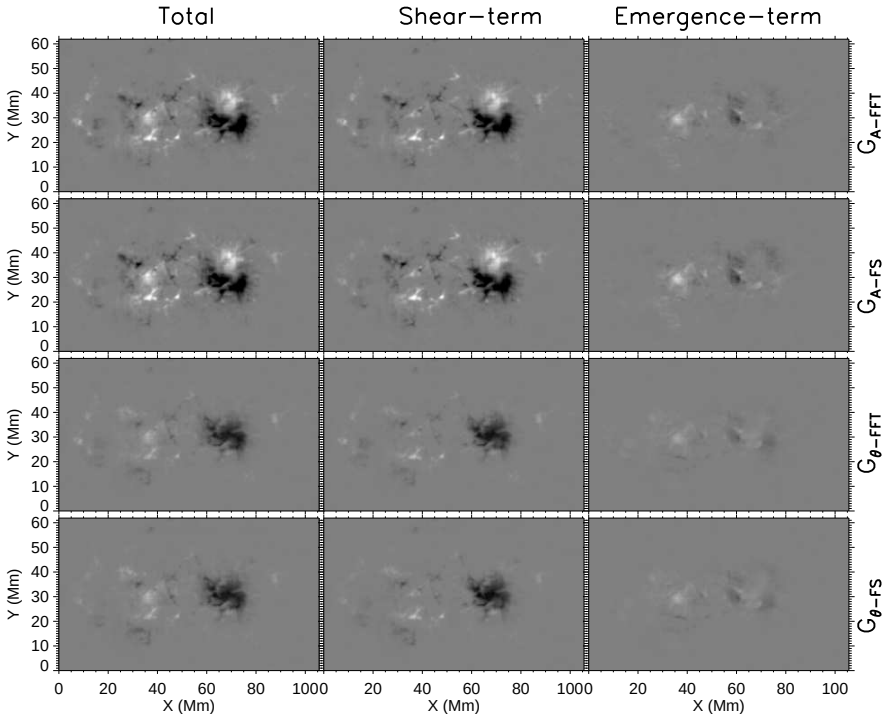

Figure 4. Helicity flux density for AR 11072. From top to bottom are $G_{\mathrm{A-FFT}}$, $G_{\mathrm{A-FS}}$, $G_{\theta-\mathrm{FFT}}$, and $G_{\theta-\mathrm{FS}}$. From left to right are total-helicity flux density, helicity flux density from shear-term, and helicity flux density from emergence-term, respectively. The images are all scaled to $\pm 1.0\times10^{19}$ Mx^2 cm^{-2} s^{-1}.

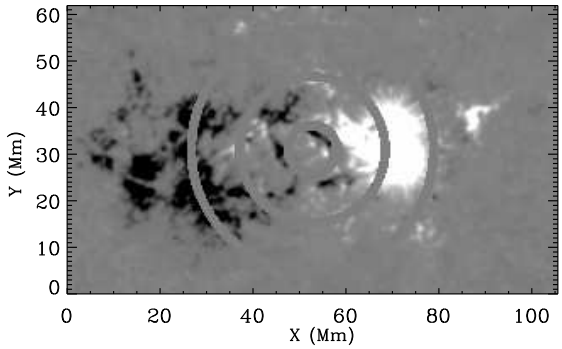

Figure 5. Normal magnetic field in AR 11072 with values in three ring-shape bands being set to be zero. It is scaled to ± 500.0 Mx cm^{-2}.

function in Equation (14). The data used is the original MHD data. The helicity flux computed from $G^{\mathrm{FFT}}_{\mathrm{A-FS}}$ converges to that computed from $G_{\mathrm{A-FS}}$ for N large enough ($N \simeq 6$) as speculated by Pariat *et al.* (2006) and Chae (2007). However, the values from these two different boundary assumptions are not identical, but can be very close when N is large enough. For example, when $N = 8$, $\mathrm{d}H_A/\mathrm{d}t|_S$

Table 1. Helicity flux calculated via different methods. The first column denotes data used. Column 2 is flux density computed from different methods. Listed in columns three – five are total, shear-term and emergence-term helicity fluxes.

Data	Type	Helicity Flux (Total) [$\mathrm{Mx^2\ s^{-1}}$]	Helicity Flux (Shear-term) [$\mathrm{Mx^2\ s^{-1}}$]	Helicity Flux (Emergence-term) [$\mathrm{Mx^2\ s^{-1}}$]
MHD Data				
	$G_{\theta-\mathrm{FS}}$	$-3.2321099 \times 10^{37}$	6.9416138×10^{36}	$-3.9262712 \times 10^{37}$
	$G_{\mathrm{A}-\mathrm{FS}}$	$-3.2321099 \times 10^{37}$	6.9416138×10^{36}	$-3.9262712 \times 10^{37}$
	$G_{\theta-\mathrm{FFT}}$	$-2.9466711 \times 10^{37}$	7.0816152×10^{36}	$-3.6548326 \times 10^{37}$
	$G_{\mathrm{A}-\mathrm{FFT}}$	$-2.9466711 \times 10^{37}$	7.0816152×10^{36}	$-3.6548326 \times 10^{37}$
HMI Data				
	$G_{\theta-\mathrm{FS}}$	$-8.9267712 \times 10^{36}$	$-9.3149077 \times 10^{36}$	3.8813650×10^{35}
	$G_{\mathrm{A}-\mathrm{FS}}$	$-8.9267712 \times 10^{36}$	$-9.3149077 \times 10^{36}$	3.8813650×10^{35}
	$G_{\theta-\mathrm{FFT}}$	$-8.2394415 \times 10^{36}$	$-8.5885657 \times 10^{36}$	3.4912417×10^{35}
	$G_{\mathrm{A}-\mathrm{FFT}}$	$-8.2394415 \times 10^{36}$	$-8.5885657 \times 10^{36}$	3.4912417×10^{35}

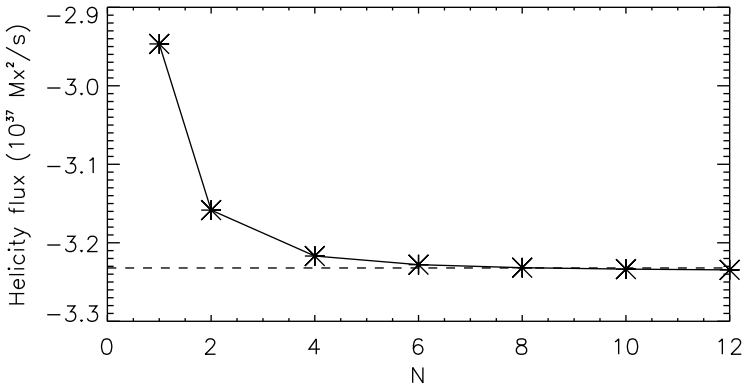

Figure 6. Helicity flux versus zero-padded data prior to applying the FFT. The original L_x (width) $\times L_y$ (height) MHD data is embedded in a new array with a size of $N \times L_x$ by $N \times L_y$. The outside of the embedded array are set to be zero for both **B** and **V**. X-axis refers to N. Y-axis is the helicity flux. The solid line with asterisks represents the helicity flux computed from $G^{\mathrm{FFT}}_{\mathrm{A}-\mathrm{FS}}$; the horizontal dashed line refers to the helicity flux from $G_{\mathrm{A}-\mathrm{FS}}$ from the original data.

from $G^{\mathrm{FFT}}_{\mathrm{A}-\mathrm{FS}}$ is $-3.2317477 \times 10^{37}$, in comparison with $\mathrm{d}H_A/\mathrm{d}t|_S$ from $G_{\mathrm{A}-\mathrm{FS}}$ that is $-3.2321099 \times 10^{37}$.

5. Conclusions

Using analysis and tests with MHD simulation data and HMI observational data, we have shown that there are no differences of computing helicity fluxes across the solar surface from two different methods, the G_A method and the G_θ method, when the boundary conditions in the Green's function used to compute G_A and G_θ are chosen consistetently. These two methods also yield essentially identical results for shear-term helicity flux and emergence-term helicity flux.

Data noise and boundary shape do not cause any differences between $\mathrm{d}H_A/\mathrm{d}t|_S$ and $\mathrm{d}H_\theta/\mathrm{d}t|_S$. If the goal is computing $\mathrm{d}H/\mathrm{d}t|_S$ there is *no material advantage* to using either G_A or G_θ. The difference found in previous studies (Pariat *et al.*, 2006; Jeong and Chae, 2007; Chae, 2007) is due to two different boundary conditions in the Green's function chosen to compute G_A and G_θ.

We have developed a fast-method for estimating G_θ based on FFT. While there are difficulties in interpreting helicity in periodic systems (Berger, 1997), the FFT provides a quick algorithm for providing reasonable estimates of $\mathrm{d}H/\mathrm{d}t|_S$ using G_A or G_θ for space-weather applications. Furthermore, given the planarization of the images and approximations of Cartesian geometry for a cutout of a spherical surface typically applied to estimate velocity for observational data, there is no clear indication of which algorithm is a more accurate estimate of $\mathrm{d}H/\mathrm{d}t|_S$. Indeed, other boundary conditions can be chosen for the Green's function such as Dirichlet (Schuck, 2008) or Neumann, or mixed.

Acknowledgements We wish to thank P. Démoulin, E. Pariat, and K. Dalmasse for valuable comments and suggestions. P. Démoulin suggested examining the size of the padding area and the helicity density computed from the FFT. YL was supported by NASA Contract NAS5-02139 (HMI) to Stanford University, and PWS was supported by NASA LWS and HGI grants. The data have been used by courtesy of NASA/SDO and the HMI science team.

References

Abbett, W.P., Fisher, G.H, Fan, Y.: 2000, *Astrophys. J.* **540**, 548.
Abbett, W.P., Fisher, G.H, Fan, Y., Bercik, D.J.: 2004, *Astrophys. J.* **612**, 557.
Berger, M.A.: 1984, *Geophys. Astrophys. Fluid Dyn.* **30**, 79.
Berger, M.A.: 1997, *J. Geophys. Res* **102**, 2637.
Berger, M.A., Ruzmaikin: 2000, *J. Geophys. Res* **105**, 10,481.
Bogomolov, V.A.:1979, *Izv. Acad. Sci. USSR Atmos. Oceanic Phys. Engl. Transl.*, **15**, 18.
Chae, J.: 2001, *Astrophys. J.* **560**, L95.
Chae, J.: 2007, *Adv. Space Res.* **39**, 1700.
Démoulin, P., Berger, M.A.: 2003, *Solar Phys.* **215**, 203. ADS:2003SoPh..215..203D, doi:10.1023/A:1025679813955.
Démoulin, P.: 2007, *Adv. Space Res.* **39**, 1674.
Hoeksema, J.T., Liu, Y., Hayashi, K., Sun, X., Schou, J., Couvidat, S., Elliot, R.C., Barnes, G., Leka, K.D.: 2012, *Solar Phys.* in preparation.
Jeong, H., Chae, J.: 2007, *Astrophys. J.* **671**, 1022.
Kimura, Y., Okamoto, H.: 1987, *J. Phys. Soc. Jpn.* **56**, 2024.
Kusano, K., Maeshiro, T., Yokoyama, T., Sakurai, T.: 2002, *Astrophys. J.* **577**, 501.
Liu, Y., Schuck, P.W.: 2012, *Astrophys. J.* in press.
Nindos, A., Zhang, J., Zhang, H.: 2003, *Astrophys. J.* **594**, 1033.
Pariat, E., Démoulin, P., Berger, A.A.: 2005, *Astron. Astrophys.* **439**, 1191.
Pariat, E., Nindos, A., Démoulin, P.: 2006, *Astron. Astrophys.* **452**, 623.
Pesnell, P.D., Thompson, B.J., Chamberlin, P.C.: 2012, *Solar Phys.* **275**, 3. ADS:2012SoPh..275....3P, doi:10.1007/s11207-011-9841-3.
Pevtsov, A.A., Maleev, V.M., Longcope, D.W.: 2003, *Astrophys. J.* **593**, 1217.
Romano, P., Pariat, E., Sicari, M., Zuccarello, F.: 2012, *Astron. Astrophys.* **525**, id.A13.
Schuck, P.W.: 2008, *Astrophys. J.* **683**, 1134.
Scherrer, P.H., Bogart, R.S., Bush, R.I., Hoeksema, J.T., Kosovichev, A.G., Schou, J., Rosenberg, W., Springer, L., Tarbell, T.D., Title, A., Wolfson, C.J., Zayer, I., MDI Engineering Team: 1995, *Solar Phys.* **162**, 129. ADS:1995SoPh..162..129S, doi:10.1007/BF00733429.
Scherrer, P.H., Schou, J., Bush, R.I., Kosovichev, A.G., Bogart, R.S., Hoeksema, J.T., Liu, Y., Duvall, T.L. Jr, Zhao, J., Title, A.M., Schrijver, C.J., Tarbell, T.D., Tomczyk, S.: 2012, *Solar Phys.* **275**, 207. ADS:2012SoPh..275..207S, doi:10.1007/s11207-011-9834-2.

Schou, J., Scherrer, P.H., Bush, R.I., Wachter, R., Couvidat, S., Rabello-Soares, M.C., Bogart, R.S., Hoeksema, J.T., Liu, Y., Duvall, T.L. Jr., Akin, D.J., Allard, B.A., Miles, J.W., Rairden, R., Shine, R.A., Tarbell, T.D., Title, A.M., Wolfson, C.J., Elmore, D.F., Norton, A.A., Tomczyk, S.: 2012, *Solar Phys.* **275**, 229. ADS:2012SoPh..275..229S, doi:10.1007/s11207-011-9842-2.

Sun, X., Hoeksema, J.T., Liu, Y., Wiegelmann, T., Hayashi, K., Chen, Q., Thalmann, J.: 2012, *Astrophys. J.*, **748**, 77.

Welsch, B.T., Abbett, W.P., De Rosa, M.L., Fisher, G.H., Georgoulis, M.K., Kusano, K., Longcope, D.W., Ravindra, B., Schuck, P.W.: 2007, *Astrophys. J.* **670**, 1434